



1 **XCO<sub>2</sub> in an emission hot-spot region: the COCCON Paris campaign 2015**

2

3 Felix R. Vogel<sup>1,a</sup>, Matthias Frey<sup>2</sup>, Johannes Stauffer<sup>3,a</sup>, Frank Hase<sup>2</sup>, Gregoire Broquet<sup>4</sup>, Irene  
4 Xueref-Remy<sup>5,a</sup>, Frederic Chevallier<sup>4</sup>, Philippe Ciais<sup>4</sup>, Mahesh Kumar Sha<sup>6,b</sup>, Pascale  
5 Chelin<sup>7</sup>, Pascal Jeseck<sup>8</sup>, Christof Janssen<sup>8</sup>, Yao Veng Te<sup>8</sup>, Jochen Groß<sup>2</sup>, Thomas  
6 Blumenstock<sup>2</sup>, Qiansi Tu<sup>2</sup> and Johannes Orphal<sup>2</sup>

7

8 1. Climate Research Division, Environment and Climate Change Canada, Toronto, Canada

9 2. Karlsruhe Institute of Technology (KIT), Institute of Meteorology and Climate Research  
10 (IMK), Karlsruhe, Germany

11 3. Thales Services, Regional Competence Center Aerospace and Science Engineering,  
12 Toulouse, France

13 4. Laboratoire des Sciences du Climat et de l'Environnement (LSCE), IPSL, CEA-CNRS-  
14 UVSQ, Université Paris-Saclay, Gif-Sur-Yvette, France

15 5. Observatoire de Haute Provence, OSU Pytheas, Saint-Michel l'Observatoire, France

16 6. Royal Belgian Institute for Space Aeronomy, Brussels, Belgium

17 7. Laboratoire Inter-Universitaire des Systèmes Atmosphériques (LISA), (CNRS UMR 7583,  
18 Université Paris Est Créteil, Université Paris Diderot, Institut Pierre Simon Laplace), Créteil,  
19 France.

20 8. Laboratoire d'Études du Rayonnement et de la Matière en Astrophysique et Atmosphères  
21 (LERMA), IPSL, Sorbonne Universités, (CNRS, PSL Research University, Observatoire de  
22 Paris), Paris, France

23

24 Previously at

25 a. Laboratoire des Sciences du Climat et de l'Environnement (LSCE), IPSL, CEA-CNRS-  
26 UVSQ, Université Paris-Saclay, Gif-Sur-Yvette, France

27 b. Karlsruhe Institute of Technology (KIT), Institute of Meteorology and Climate Research  
28 (IMK), Karlsruhe, Germany

29

30 *Correspondence to: Felix R. Vogel (Felix.Vogel@canada.ca)*

31

32 **Abstract.** Providing timely information on urban Greenhouse-Gas (GHG) emissions and  
33 their trends to stakeholders relies on reliable measurements of atmospheric concentrations  
34 and the understanding of how local emissions and atmospheric transport influence these  
35 observations.

36 Portable Fourier Transform Infra-Red (FTIR) spectrometers were deployed at 5 stations in  
37 the Paris metropolitan area to provide column-averaged concentrations of CO<sub>2</sub> (XCO<sub>2</sub>)



38 during a field campaign in spring of 2015. Here, we describe and analyze the variations of  
39 XCO<sub>2</sub> observed at different sites and how they changed over time. We find that observations  
40 upwind and downwind of the city centre differ significantly in their XCO<sub>2</sub> concentrations,  
41 while the overall variability of the daily cycle is similar, i.e., increasing during night-time with  
42 a strong decrease (typically 2-3 ppm) during the afternoon.

43 An atmospheric transport model framework (CHIMERE-CAMS) was used to simulate XCO<sub>2</sub>  
44 and predict the same behaviour seen in the observations, which supports key findings, e.g.  
45 that even in a densely populated region like Paris (over 12 Million people), biospheric uptake  
46 of CO<sub>2</sub> can be of major influence on daily XCO<sub>2</sub> variations. Despite a general offset between  
47 modelled and observed XCO<sub>2</sub>, the model correctly predicts the impact of the meteorological  
48 parameters (e.g. wind direction and speed) on the concentration gradients between different  
49 stations. Looking at the local gradients of XCO<sub>2</sub> for upwind and downwind station pairs,  
50 which is less sensitive to changes in XCO<sub>2</sub> regional background conditions, we find the  
51 model-data agreement significantly better. Our modelling framework indicates that the local  
52 XCO<sub>2</sub> gradient between the stations is dominated by the fossil fuel CO<sub>2</sub> signal of the Paris  
53 metropolitan area. This highlights the usefulness of XCO<sub>2</sub> observations to help optimise  
54 future urban GHG emission estimates.

55

## 56 1 Introduction

57 Atmospheric background concentrations of CO<sub>2</sub> measured since 1958 in Mauna Loa, USA,  
58 have passed the symbolic milestone of 400 ppm (monthly mean) as of 2013 [Jones 2013].  
59 Properly quantifying fossil fuel CO<sub>2</sub> emissions (FFCO<sub>2</sub>) can contribute to define effective  
60 climate mitigation strategies. Focussing our attention on cities is a critical part of this  
61 endeavour as emissions from urban areas are currently estimated to represent from 53 % to  
62 87 % of global FFCO<sub>2</sub>, depending on the accounting method considered, and are predicted  
63 to increase further [IPCC-WG3 2014, IEA 2008, Dhakal 2009]. As stated in the IPCC 5<sup>th</sup>  
64 assessment report, “*current and future urbanisations trends are significantly different from*  
65 *the past*” and “*no single factor explains variations in per-capita emissions across cities and*  
66 *there are significant differences in per capita greenhouse gas (GHG) emissions between*  
67 *cities within a single country*” [IPCC-WG3 2014]. The large uncertainty of the global  
68 contribution of urban areas to CO<sub>2</sub> emissions today and in the future is why a new  
69 generation of city-scale observing and modelling systems are needed.

70 In recent years, more and more atmospheric networks have emerged that observe GHG  
71 concentrations using the atmosphere as a large-scale integrator, for example in Paris  
72 (France), Indianapolis (USA), and Toronto (Canada). The air measured at in-situ ground-  
73 based stations is considered to be representative of surface CO<sub>2</sub> fluxes of a larger  
74 surrounding area (1 km<sup>2</sup>-10000 km<sup>2</sup>) [e.g., Bréon et al. 2015, Xueref-Remy et al, 2018,



75 Turnbull et al. 2015, Vogel et al. 2013]. If CO<sub>2</sub> measurements are performed both up-wind  
76 and downwind of a city, the concentration gradient between the two locations is influenced  
77 by the local net emission strength between both sites and atmospheric mixing [Xueref-Remy  
78 et al, 2018, Bréon et al. 2015, Turnbull et al. 2015]. To derive quantitative flux estimates,  
79 measured concentration data are typically assimilated into numerical atmospheric transport  
80 models which calculate the impact of atmospheric mixing on concentration gradients for a  
81 given flux space-time distribution. Such a data assimilation framework implemented for Paris  
82 with three atmospheric CO<sub>2</sub> measurement sites [Xueref-Remy et al, 2018] previously allowed  
83 deriving quantitative estimates of monthly emissions and their uncertainties over one year  
84 [Staufer et al. 2016].

85 Space-borne measurements of the column-average dry air mole fraction of CO<sub>2</sub> (XCO<sub>2</sub>) are  
86 increasingly considered for the monitoring of urban CO<sub>2</sub>. This potential was shown with  
87 OCO-2 and GOSAT XCO<sub>2</sub> measurements, even though the spatial coverage and temporal  
88 sampling frequency of these two instruments were not optimized for FFCO<sub>2</sub> [Kort et al.,  
89 2012, Janardanan et al. 2016, Schwandner et al. 2017], while other space-borne sensors  
90 dedicated to FFCO<sub>2</sub> and with an imaging capability are in preparation [O'Brien et al, 2016,  
91 Broquet et al. 2017]. Important challenges of satellite measurements are that they are not as  
92 accurate as in-situ ones, having larger by systematic errors, while the XCO<sub>2</sub> gradients in the  
93 column are typically 7-8 times smaller than in the boundary layer. Another difficulty of space-  
94 borne imagery with passive instruments is that they will only sample city XCO<sub>2</sub> plumes  
95 during clear sky conditions at around mid-day.

96 The recent development of a robust portable ground-based FTIR (Fourier Transform  
97 InfraRed) spectrometer as described in Gisi et al. [2012] and Hase et al. [2015] (EM27/SUN,  
98 Bruker Optik, Germany) greatly facilitates the measurement of XCO<sub>2</sub> from the surface, with  
99 better accuracy than from space and with the possibility of continuous daytime observation  
100 during clear sky conditions. Typical compatibility (uncorrected bias) of the EM27/SUN  
101 retrievals of the different instruments in a local network is better than 0.01 % (i.e. ~ 0.04 ppm)  
102 after a careful calibration procedure and a harmonized processing scheme for all  
103 spectrometers [Frey et al. 2015]. The Collaborative Carbon Column Observing Network  
104 (COCCON) [Frey et al. 2018] intends to offer such a framework for operating the  
105 EM27/SUN. This type of spectrometers therefore represents a remarkable opportunity to  
106 document XCO<sub>2</sub> variability in cities as a direct way to estimate FFCO<sub>2</sub> [Hase et al. 2015] or  
107 in preparation of satellite missions.

108 When future low-Earth-orbit operational satellites with imaging passive spectrometers of  
109 suitable capabilities to invert FFCO<sub>2</sub> will sample different cities, this will likely be limited to  
110 clear sky conditions and at a time of the day close to local noon. Increasing the density of  
111 the COCCON network around cities will allow to evaluate those XCO<sub>2</sub> measurements and to



112 monitor XCO<sub>2</sub> during the early morning and afternoon periods, which will not be sampled  
113 with satellites, except from geostationary orbit [Butz et al., 2015].

114 This study focuses on the measurements of XCO<sub>2</sub> from ground based EM27/SUN  
115 spectrometers deployed within the Paris metropolitan area during a field campaign in the  
116 spring of 2015, and modelling results. This campaign can be seen as a demonstration of the  
117 COCCON network concept applied to the quantification of an urban FFCO<sub>2</sub> source. Several  
118 spectrometers were operated by different research groups, while closely following the  
119 common procedures suggested by Frey et al. [2015]. The paper is organised as follows.  
120 After the instrumental and modelling setup descriptions of section 2, the observations of the  
121 field campaign and the modelling results will be presented in section 3. Results are  
122 discussed in section 4 together with the study conclusions.

123

## 124 **2 Methods and materials**

### 125 **2.1 Description of study area and field campaign design**

126 During the COCCON field campaign (April 28th to May 13th, 2015) five portable FTIR  
127 spectrometers (EM27/SUN, Bruker Optik, Karlsruhe, Germany) were deployed in the  
128 Parisian region (administratively known as *Île-de-France*) and within the city of Paris. The  
129 campaign was conducted in early spring as the cloud cover is typically low in April and May  
130 and the time between sunrise and sunset is more than 14 hours.

131 The Paris metropolitan area houses over 12 million people, with about 2.2 million inhabiting  
132 the city of Paris. This urban region is the most densely populated in France with ~1000  
133 inhabitants/km<sup>2</sup> and over 21000 inhabitants/km<sup>2</sup> for the city of Paris itself [INSEE 2016 -  
134 <https://www.insee.fr/fr/statistiques>]. The estimated CO<sub>2</sub> emissions from the metropolitan  
135 region are 39 Mt/year with on-road traffic emissions and residential and the tertiary (i.e.  
136 commercial) sector as main sources (accounting for over 75 %), and minor contributions  
137 from other sectors such as industrial sources and airports [AIRPARIF 2016]. It was crucial to  
138 understand the spatial distribution of these CO<sub>2</sub> sources to optimally deploy the COCCON  
139 spectrometers. To this end a 1 km emission model for France by IER (Institut fuer  
140 Energiewirtschaft und Rationelle Energieanwendung, University of Stuttgart, Germany) was  
141 used as a starting point [Latoska 2009]. This emission inventory is based on the available  
142 activity data such as, e.g., traffic counts, housing statistics, or energy use, and the temporal  
143 disaggregation was implemented according to Vogel et al. [2013]. In brief, the total  
144 emissions of the IER model were re-scaled to match the temporal factors for the different  
145 emission sectors according to known national temporal emission profiles.

146 To quantify the impact of urban emissions on XCO<sub>2</sub>, the FTIR instruments were deployed  
147 along the dominant wind directions in this region in spring, i.e., southwesterly [Staufner et al  
148 2016], in order to maximize the likelihood to capture upwind and downwind air masses (see



149 Figure 1). The two southwesterly sites (GIF and RES) are located in a less densely  
150 populated area, where emissions are typically lower than in the city centre, where the station  
151 JUS is located. The data in Fig. 1 show that the densest FFCO<sub>2</sub> emission area extends  
152 northwards and eastwards. The two Northwesterly sites (PIS and MIT) were placed  
153 downwind of this area. All instruments were operated manually and typically started for  
154 operations around 7-8 am local time from which they continuously observe XCO<sub>2</sub> until 5-6  
155

## 156 2.2 Instrumentation, calibration, and data processing

157 The EM27/SUN is a portable FTIR spectrometer which has been described in detail in, e.g.,  
158 Gisi et al. [2012] and Frey et al. [2015]. Here, only a short overview is given. The centre  
159 piece of the instrument is a Michelson interferometer which splits up the incoming solar  
160 radiation into two beams. After inserting a path difference between the beams, the partial  
161 beams are recombined. The modulated signal is detected by an InGaAs detector covering  
162 the spectral domain from 5000 to 11000 cm<sup>-1</sup> and is called an interferogram. As the  
163 EM27/SUN analyzes solar radiation, it can only operate in daylight sunny conditions. A  
164 Fourier transform of the interferogram generates the spectrum and a DC correction is  
165 applied to remove the background signal and only keep the AC signal (see Keppel-Aleks et  
166 al. [2007]). A numerical fitting procedure (PROFFIT code) [Schneider and Hase et al., 2009]  
167 then retrieves column abundances of the concentrations of the observed gases from the  
168 spectrum. The single-channel EM27/SUN is able to measure total columns of O<sub>2</sub>, CO<sub>2</sub>, CH<sub>4</sub>  
169 and H<sub>2</sub>O. The ratio over the observed O<sub>2</sub> column, assumed to be known and constant,  
170 delivers the column-averaged trace gas concentrations of XCO<sub>2</sub>, XCH<sub>4</sub> in μmol / mol dry air,  
171 with a temporal resolution of one minute. XCO<sub>2</sub> is the dry air mole fraction of CO<sub>2</sub>, defined as  
172  $XCO_2 = \text{Column}[CO_2] / \text{Column}[\text{Dry Air}]$ . Applying the ratio over the observed oxygen (O<sub>2</sub>)  
173 column reduces the effect of various possible systematic errors; see Wunch et al. (2011).

174 In order to correctly quantify small differences in XCO<sub>2</sub> columns between Paris city upstream  
175 and downstream locations, measurements were performed with the five FTIR instruments  
176 side by side before and after the campaign, as we expect small calibration differences  
177 between the different instruments due to slightly different alignment for each individual  
178 spectrometer. These differences are constant over time and can be easily accounted for by  
179 applying a calibration factor for each instrument. Previous studies showed that the  
180 instrument specific corrections are well below 0.1 % for XCO<sub>2</sub> [Frey et al. 2015, Chen et al.  
181 2016] and are stable for individual devices. The 1-sigma precision for XCO<sub>2</sub> is in the order of  
182 0.01 % - 0.02 % (< 0.08 ppm) e. g. [Gisi et al. 2012, Chen et al. 2016, Hedelius et al. 2016,  
183 Klappenbach et al. 2015]. The calibration measurements for this campaign were performed  
184 in Karlsruhe w.r.t. the Total Carbon Column Observing Network (TCCON) [Wunch et al.  
185 2011] spectrometer at the Karlsruhe Institute of Technology (KIT), Germany for 7 days



186 before the Paris campaign between April 9<sup>th</sup> and 23<sup>rd</sup>, and after the campaign on May 18<sup>th</sup>  
187 until 21<sup>st</sup>.

188 Figure 2 (left panel) shows the XCO<sub>2</sub> time series of the calibration campaign, where small  
189 offsets between the instruments raw data are visible. As these offsets are constant over  
190 time, a calibration factor for each instrument can be easily applied; actually these are the  
191 calibration factors previously found for the Berlin campaign [Frey et al. 2015]. These factors  
192 are given in Table 2, where all EM27/SUN instruments are scaled to match instrument No. 1.  
193 The calibrated XCO<sub>2</sub> values for April 15<sup>th</sup> are shown in Fig. 2 (right panel). None of the five  
194 instruments that participated in the Berlin campaign show any significant drift; in other words,  
195 the calibration factors found one year before were still applicable. This is an impressive  
196 demonstration of the instrument stability stated in section 2.2, especially as several  
197 instruments (Nos. 1, 3, 5) were used in another campaign in Northern Germany in the  
198 meantime. The EM27/SUN XCO<sub>2</sub> measurements can be made traceable to the WMO  
199 international scale for in-situ measurements by comparison with measurements of a  
200 collocated spectrometer from the TCCON. TCCON instruments are calibrated against in-situ  
201 standards by aircraft and aircore measurements [Wunch et al. 2010, Messerschmidt et al.  
202 2012] performed using the WMO scale.

203 During the campaign and for the calibration measurements we recorded double-sided  
204 interferograms with 0.5 cm<sup>-1</sup> spectral resolution. Each measurement of 58 s duration  
205 consisted of 10 scans using a scanner velocity of 10 kHz. For precise timekeeping, we used  
206 GPS sensors for each spectrometer.

207 In-situ surface pressure data used for the analysis of the calibration measurements  
208 performed at KIT have been recorded at the co-located meteorological tall tower. During the  
209 campaign, a MHD-382SD data-logger recorded local pressure, temperature and relative  
210 humidity at each station. The analysis of the trace gases from the measured spectra for the  
211 calibration measurements has been performed as described by Frey et al. [2015]. For the  
212 campaign measurements we assume a common vertical pressure-temperature profile for all  
213 sites, provided by the model, so that the surface pressure at each spectrometer only differs  
214 due to different site altitudes. The 3-hourly temperature profile from the European Centre for  
215 Medium-Range Weather Forecasts (ECMWF) operational analyses interpolated for site JUS  
216 located in the centre of the array was used for the spectra analysis at all sites. The individual  
217 ground-pressure was derived from site altitudes and pressure measurements performed at  
218 each site.

219 Before and after the Paris campaign, side by side comparison measurements were  
220 performed with all 5 EM27/SUN spectrometers and the TCCON spectrometer operated in  
221 Karlsruhe at KIT. All spectrometers were placed on the top of the IMK office building North of  
222 Karlsruhe. The altitude is 133 m above sea level (a.s.l.), coordinates are 49.09° N and 8.43°



223 E. The processing of the Paris raw observations (measured interferograms) were performed  
224 as described by Gisi et al. [2012] and Frey et al. [2015] for the Berlin campaign: spectra  
225 were generated applying a DC correction, a Norton-Beer medium apodization function and a  
226 spectral resampling of the sampling grid resulting from the FFT on a minimally sampled  
227 spectral grid. PROFFWD was used as the radiative transfer model and PROFFIT as the  
228 retrieval code.

229

### 230 **2.3 Atmospheric transport modelling framework**

231 We used the chemistry transport model CHIMERE (Menut et al., 2013) to simulate CO<sub>2</sub>  
232 concentrations in the Paris area. More specifically, we used the CHIMERE configuration  
233 over which the inversion system of Bréon et al. [2015] and Staufer et al. [2016] was built to  
234 derive monthly to 6-hour mean estimates of the CO<sub>2</sub> Paris emissions. Its horizontal grid, and  
235 thus its domain and its spatial resolution, are illustrated in Figure 3. It has a 2 × 2 km<sup>2</sup> spatial  
236 resolution for the Paris region, and 2 × 10 km<sup>2</sup> and 10 × 10 km<sup>2</sup> spatial resolutions for the  
237 surroundings. It has 20 vertical hybrid pressure-sigma (terrain-following) layers that range  
238 from the surface to the mid-troposphere, up to 500 hPa. It is driven by operational  
239 meteorological analyses of the ECMWF Integrated Forecasting System, available at an  
240 approximately 15 × 15 km<sup>2</sup> spatial resolution and 3 h temporal resolution.

241 In this study the CO<sub>2</sub> simulations are based on a forward run over April 25<sup>th</sup> - May 12<sup>th</sup> 2015  
242 with this model configuration; we do not assimilate atmospheric CO<sub>2</sub> data and so no  
243 inversion for surface fluxes was conducted. In the Paris area (the Île-de-France  
244 administrative region), hourly anthropogenic emissions are given by the IER inventory, see  
245 section 2.1. The anthropogenic emissions in the rest of the domain are prescribed from the  
246 EDGAR V4.2 database for the year 2010 at 0.1° resolution [Olivier and Janssens-Maenhout  
247 et al., 2012]. In the whole simulation domain, the natural fluxes (the Net Ecosystem  
248 Exchange: NEE) are prescribed using simulations of C-TESSSEL, which is the land-surface  
249 component of the ECMWF forecasting system [Boussetta et al., 2013], at a 3 hourly and 15  
250 × 15 km<sup>2</sup> resolution. Finally, the CO<sub>2</sub> boundary conditions at the lateral and top boundaries of  
251 the simulation domain and the simulation CO<sub>2</sub> initial conditions on April 25<sup>th</sup> 2015 are  
252 prescribed using the CO<sub>2</sub> forecast issued by the Copernicus Atmosphere Monitoring Service  
253 (CAMS, <http://atmosphere.copernicus.eu/>) at a ~15 km global resolution [Agustí-Panareda  
254 et al., 2014].

255 The CHIMERE transport model is used to simulate the XCO<sub>2</sub> data. However, since the  
256 model does not cover the atmosphere up to its top, the CO<sub>2</sub> fields from CHIMERE are  
257 complemented with that of the CAMS CO<sub>2</sub> forecasts from 500 hPa to the top of the  
258 atmosphere to derive total column concentrations. The derivation of modelled XCO<sub>2</sub> at the



259 sites, involves obtaining a kernel-smoothed CO<sub>2</sub> profile of CHIMERE and CAMS and vertical  
260 integration of these smoothed profiles, weighted by the pressure at the horizontal location of  
261 the sites.

262 The parametrisation used to smooth modelled CO<sub>2</sub> profiles approximates the sensitivity of  
263 the EM27/sun CO<sub>2</sub> retrieval is a function of pressure and sun elevation. Between 1000 hPa  
264 and 480 hPa, a linear dependency of the instrument averaging kernels on solar zenith angle  
265 ( $\theta$ ) is assumed with boundary values following Frey et al. [2015]:

266

$$267 \quad (1a) \quad k(480 \text{ hPa}) = 1.125$$

$$268 \quad (1b) \quad k(1000 \text{ hPa}) = 1.0 + 0.45 s^3$$

269

270 where  $s = \theta/90^\circ$ .  $k$ . Approximate averaging kernels are obtained by linear interpolation to the  
271 pressure levels of CHIMERE and CAMS, respectively. If  $p > 1000$  hPa,  $k$  is linearly  
272 extrapolated. Above 480 hPa ( $p < 480$  hPa), the averaging kernels can be approximated by

273

$$274 \quad (2) \quad k(u, s) = 1.125 - 0.6 u^3 - 0.4 u s^3$$

275

276 where  $u$  is  $(480 \text{ hPa} - p) / 480$ . The kernel-smoothed CO<sub>2</sub> profile,  $CO_{2\_model}^s$ , is obtained by

277

$$278 \quad (3) \quad CO_{2\_model}^s = \mathbf{K} CO_{2\_model} + (\mathbf{I} - \mathbf{K}) CO_2^a$$

279

280

281 where  $CO_{2\_model}$  is the modelled CO<sub>2</sub> profile by CHIMERE or CAMS,  $\mathbf{I}$  the identity matrix and  
282  $\mathbf{K}$  is a diagonal matrix containing the averaging kernels  $k$ . The a priori CO<sub>2</sub> profile,  $CO_2^a$ , is  
283 provided by the **Whole Atmosphere Community Climate Model** (WACCM) model (version  
284 6) and interpolated to the pressure levels of CHIMERE and CAMS.  $CO_{2\_model}^s$  is the  
285 appropriate CO<sub>2</sub> profile to calculate modelled XCO<sub>2</sub> at the location of the sites.

286

287 For a given site, the simulated XCO<sub>2</sub> data are thus computed from the vertical profile of this  
288 site as:

289

$$290 \quad (3) \quad XCO_{2\_CHIMERE} = \frac{1}{p_{surf}} \int_{p_{surf}}^{p_{top\_CHIM}} CO_{2\_CHIM}^s dp + \int_{p_{top\_CHIM}}^{P=0mbar} CO_{2\_CAMs}^s dp$$

291

292 where  $p_{surf}$  is the surface pressure,  $p_{top\_CHIM} = 500$  hPa the pressure corresponding to the top  
293 boundary of the CHIMERE model, and  $CO_{2\_CHIM}^s$  and  $CO_{2\_CAMs}^s$  are the smoothed CO<sub>2</sub>





294 concentrations of CHIMERE and CAMS respectively. For comparison we also calculated  
295 XCO<sub>2</sub> at a lower spatial resolution with the CAMS data alone as:

296

$$297 \quad (4) \quad XCO_{2\_CAMS} = \int_{P_{surf}}^{P=0mbar} CO_{2\_CAMS}^S dP$$

298

### 299 **3 Results and discussion**

#### 300 **3.1 Observations**

##### 301 **3.1.1 Meteorological conditions and data coverage/instrument performance.**

302 During the measurement campaign (April 28<sup>th</sup> until May 13<sup>th</sup>, 2015), meteorological  
303 conditions were a major limitation for the availability of XCO<sub>2</sub> observations. Useful  
304 EM27/SUN measurements require direct sunlight and low wind speeds typically yield higher  
305 local XCO<sub>2</sub>. Most of the time during the campaign conditions were partly cloudy and turbid,  
306 and so successful measurements at high solar zenith angle (SZA) were rare. Therefore, the  
307 data coverage between April 28<sup>th</sup> and May 3<sup>rd</sup> is limited (see Table 3). As is typical for spring  
308 periods in Paris, the temperature and the wind direction vary and display less synoptic  
309 variations than in winter. The dominant wind directions were mostly northeasterly at the  
310 beginning of the campaign and mostly southeasterly during the second half of the campaign.  
311 We find that the wind speeds during daytime nearly always surpass 3 m s<sup>-1</sup>, which has been  
312 identified by Breon et al. [2015] and Staufer et al. [2016] as the cut-off wind speed above  
313 which the atmospheric transport model CHIMERE performs best in modelling CO<sub>2</sub>  
314 concentration gradients in the mixed layer.

315 Despite some periods with unfavourable conditions, more than 10,000 spectra were  
316 retrieved among the five deployed instruments. The quality of the spectra for each day was  
317 rated according to the overall data availability. The best measurement conditions prevailed  
318 for the period between May 7<sup>th</sup> and May 12<sup>th</sup>.

319

##### 320 **3.1.2 Observations of XCO<sub>2</sub> in Paris**

321 The observed XCO<sub>2</sub> in the Paris region for all sites (10415 observations) ranges from 397.27  
322 to 404.66 ppm with a mean of 401.26 ppm (a median of 401.15 ppm) and a standard  
323 deviation of 1.04 ppm for 1-minute averages. We find that all sites exhibit very similar diurnal  
324 behaviours with a clear decrease of XCO<sub>2</sub> during daytime and a noticeable day to day  
325 variability as seen in Figure 4. This is to be expected as they are all subject to very similar  
326 atmospheric transport in the boundary layer height and to similar large-scale influences, i.e.,  
327 surrounding with stronger natural fluxes or air mass exchange with other regions at synoptic  
328 time scales. However, observed XCO<sub>2</sub> concentrations at the upwind sites for our network  
329 remain clearly higher from sites that are downwind of Paris (see Figure 4). This indicates



330 that the influence of urban emissions is detectable with this network configuration under  
331 favourable meteorological conditions. By comparing the different daily variations in Fig. 5, it  
332 is apparent that the day-to-day variations observed at the two southwesterly (typically  
333 upwind) sites GIF and RES are approximately 1 ppm, with both sites exhibiting similar diurnal  
334 variations throughout the campaign period. This can be expected as their close vicinity  
335 would suggest that they are sensitive to emissions from similar areas and to concentrations  
336 of air masses arriving from the southwest.

337 The typical decrease in  $XCO_2$  found over the course of a day is about 2 to 3 ppm. This  
338 decrease can only be driven by (natural) sinks of  $CO_2$ , which can be expected to be very  
339 strong as our campaign took place after the start of the growing season in Europe for most  
340 of southern and central Europe [Roetzer and Chmielewski 2001].

341 The observations at the site located in Paris (JUS) displays similarly low day-to-day  
342 variations and a clear decrease in  $XCO_2$  over the course of the day. The latter feature  
343 indicates that even in the dense city centre,  $XCO_2$  is primarily representative of a large  
344 footprint like in other areas of the globe [Keppel-Aleks, 2011] and is not as critically affected  
345 by local emissions than in-situ measurements [Breon et al. 2015, Ammoura et al. 2016]. It is  
346 also apparent that the decrease in  $XCO_2$  (the slope) during the afternoon for April 28<sup>th</sup> and  
347 29<sup>th</sup> as well as May 7<sup>th</sup> and 10<sup>th</sup> is noticeably smaller than at other days during this  
348 campaign. As  $XCO_2$  is not sensitive to vertical mixing, this has to be caused by different  $CO_2$   
349 sources and sinks acting upon the total column arriving at JUS.

350 The two northeasterly (typically downwind) sites PIS and MIT show a markedly larger day-to-  
351 day spread in the background as well as strongly changing slopes for the diurnal  $XCO_2$   
352 decrease. For these sites the exact wind direction is critical as they can be downwind of the  
353 city centre that has a much higher emission density or less dense suburbs (see Fig. 1).

354

### 355 3.1.3 Gradients in observed $XCO_2$

356 In order to focus more on the impact of local emissions and less on that of background  
357 influences in our analysis of  $XCO_2$ , we choose to study the spatial gradients ( $\Delta$ ) between  
358 different sites. Ideal conditions were sampled during May 7<sup>th</sup>, with predominantly  
359 southwesterly winds, and on May 10<sup>th</sup> with southerly winds. We can see in Fig. 6 that all  
360 sites are, on average, elevated compared to RES, chosen as reference here as it was  
361 upwind of Paris during the measurement period. The observations from GIF only show  
362 minimal differences with RES, and  $\Delta$  increases between PIS, JUS and MIT and RES to  
363 reach 1 to 1.5 ppm. During southwesterly winds, MIT is downwind of most of the densest  
364 part of the Paris urban area, and JUS is impacted by emissions of neighborhoods to the  
365 southwest. The site of PIS is still noticeably influenced by the city centre but, as can be seen  
366 in Fig. 1, we likely do not catch the plume of the most intense emissions but rather from the



367 suburbs. On May 10<sup>th</sup>, with its dominant southerly winds, the situation is markedly different.  
368 While GIF is still only slightly elevated, the XCO<sub>2</sub> enhancement at MIT is significantly lower  
369 and quite similar to JUS for large parts of the day. The highest  $\Delta$ XCO<sub>2</sub> can now be observed  
370 at PIS, again typically ranging from 1 to 1.5 ppm. As seen in Fig. 1, PIS is now directly  
371 downwind of the densest emission area, while MIT is only exposed to CO<sub>2</sub> emissions from  
372 the eastern outskirts of Paris.

373 It is also important to note that the impact of the local biosphere that is assumed to cause  
374 the strong decrease in XCO<sub>2</sub> during the day is not seen on both days for these spatial  
375 gradients. For a more comprehensive interpretation of these observations the use of a  
376 transport model (as described in section 2.3) is necessary.

377

## 378 **3.2 Modelling**

### 379 **3.2.1 Model performance**

380 Before interpreting the modelled XCO<sub>2</sub> we need to evaluate the performance of the chosen  
381 atmospheric transport model framework as described in section 2.3. Comparing it to  
382 meteorological observations (wind speed and wind direction) at GIF in Fig. 7, we find that  
383 CHIMERE predicts these variables well throughout the duration of the campaign. Changes in  
384 wind speed direction and speed are reproduced with a slight overestimation at low wind-  
385 speeds (>1m/s). Besides the meteorological forcing, the model performance can also be  
386 expected to depend on the chosen model resolution. Therefore, we compared XCO<sub>2</sub> at JUS  
387 calculated based on the coarser resolution atmospheric transport and flux framework CAMS  
388 (15 km), and the higher resolution emission modelling input for the framework based on  
389 CHIMERE (2 km) for the inner domain and on CAMS boundary conditions (see Fig. 8). We  
390 find that the coarser model displays similar inter-daily variations, but that the high-resolution  
391 model modifies the modelling results on shorter time-scales. We find that the afternoon  
392 XCO<sub>2</sub> decreases are often more pronounced in CHIMERE. Only the high-resolution will be  
393 considered and referred to in the following.

394

395 The impact of using different flux maps (fossil fuel CO<sub>2</sub> and biosphere models) on the  
396 modelled XCO<sub>2</sub> can unfortunately not be explicitly investigated here as only one high-  
397 resolution (1 km) emission product was available for this study (see section 2.3).

398

### 399 **3.2.2 Modelled XCO<sub>2</sub> and its components**

400 The modelled XCO<sub>2</sub> for the five sites (Fig. 9) co-evolves over the period of the campaign with  
401 occurrences of significant differences. This was already seen with the measurements, but the  
402 model allows looking at the full time series. The model reveals clear daily cycles of XCO<sub>2</sub>,  
403 with an accumulation during night-time and a decrease during daytime. Despite a good



404 general agreement of modelled  $XCO_2$  at all sites for, e.g., the timing of daily minima and  
405 their synoptic changes, differences in  $XCO_2$  are observed between the sites for many days.  
406 Typically the northeasterly sites (PIS, MIT) show an enhancement in  $XCO_2$  compared to the  
407 southwesterly sites (GIF, RES).

408 To understand the synoptic and diurnal variations of  $XCO_2$ , we analyzed the contribution of  
409 different sources (and sinks) of  $CO_2$ , namely the net ecosystem exchange (NEE), the fossil  
410 fuel  $CO_2$  emissions (FFCO<sub>2</sub>), and the boundary conditions (BC), i.e., the variations of  $CO_2$   
411 not caused by fluxes within our domain (the example of JUS is given in Fig. 10; see the  
412 supplement for the other sites). The day-to-day variability of modelled  $XCO_2$  is dominated by  
413 changing boundary conditions and coincides with synoptic weather changes. The strong  
414 daily decrease in  $XCO_2$  can be directly linked to NEE, which leads to a decrease of ~1 ppm  
415 (but up to 4 ppm) during the day. The  $XCO_2$  from fossil fuel emissions causes significant  
416 enhancements compared to the background, but is often compensated by NEE. During short  
417 periods, fossil fuel emissions can however lead to enhancements of up to 4 ppm.

418

### 419 3.2.3 Modelled $\Delta XCO_2$ gradients and its components

420 To be able to assess the impact of local sources and reduce the influence of NEE and BC on  
421 the modelled signals, we analyse the  $XCO_2$  gradient (i.e. station-to-station difference) with  
422 RES being taken as reference. In Fig. 11 we compare  $\Delta$  along a south-north direction. For  
423 the modelled  $\Delta$  we can see that MIT shows a positive value during the campaign period  
424 whenever the predominant wind direction was southwesterly (grey shaded areas). We also  
425 find that  $\Delta$  between JUS and RES was both negative and positive during the campaign, and  
426 predominantly negative between MIT and JUS. When split into FFCO<sub>2</sub>, BC and NEE  
427 components, we can clearly see that the total  $\Delta$  is dominated by FF causing  $XCO_2$  offsets of  
428 up to 4 ppm, but more typically 1 ppm gradients are observed. Gradients can also change  
429 rapidly (within a few hours) if the wind direction changes, for example on May 1<sup>st</sup> and May  
430 12<sup>th</sup>. This highlights the fact that, during such conditions, we cannot assume a simple  
431 upwind-downwind interpretation of our sites. As expected, the contributions from BC and  
432 NEE are generally greatly reduced when analysing  $\Delta XCO_2$ . The most important impact of  
433 NEE on the  $XCO_2$  gradients of -1ppm and +1ppm can be seen on May 8<sup>th</sup> and May 11<sup>th</sup>,  
434 respectively. This means that, despite greatly reducing the impact of NEE on average, the  
435 contribution of NEE cannot be fully ignored. BC is an overall negligible contribution to  
436  $\Delta XCO_2$ , even though it reaches -0.4 ppm on May 11<sup>th</sup>.

437

## 438 3.3 Model data and observations comparison

### 439 3.3.1 $XCO_2$



440 A comparison of modelled and observed  $XCO_2$  is of course limited to the relatively short  
441 periods when observations are available. Over these periods. we observe that the main  
442 features of the modelled and observed  $XCO_2$  are comparable. The daytime variations are  
443 well reproduced by the model and the general relative concentrations between sites are  
444 preserved, e.g., the highest values for  $XCO_2$  at MIT are on May 9<sup>th</sup> and highest  $XCO_2$  for PIS  
445 are later on May 10<sup>th</sup> and May 11<sup>th</sup> as seen in Figure 12. We can also see a general issue in  
446 reproducing the background  $XCO_2$  for each day in the model as observed  $XCO_2$  is  
447 significantly lower by typically between 1 to 2 ppm. We also see that the timing of the daily  
448 minima is not fully covered in the observed data as it typically happens after sunset and  
449 cessation of biosphere uptake.

450

### 451 3.3.2 $\Delta XCO_2$

452 Due to the prevailing southeasterly wind conditions, we can compare  $XCO_2$  at the typical  
453 downwind sites (PIS, MIT) relative to the mostly upwind sites (RES, GIF) and expect  
454 elevated  $XCO_2$  downwind. We find that the  $\Delta XCO_2$  of PIS relative to RES falls along the 1:1  
455 line with a slope of  $1.07 \pm 0.09$  with a Pearson's R of 0.8. Negative  $\Delta XCO_2$  values, seen in  
456 Fig. 13, are associated with meteorological conditions when winds come from northerly or  
457 easterly directions, i.e., the roles of normal upwind and downwind sites are reversed. The  
458 gradient of  $XCO_2$  MIT relative to RES has a significantly lower range for modelled  $XCO_2$   
459 while the observed range of  $XCO_2$  is similar to PIS. The slope of observed to modelled  
460  $\Delta XCO_2$  is  $1.72 \pm 0.06$  with a Pearson's R of 0.96. This points to a significant underestimation  
461 of the impact of urban sources on the MIT-RES gradient, which is also visible in the more  
462 negative  $\Delta XCO_2$  during northerly wind conditions. This could indicate that the spatial  
463 distribution of our emissions prior should be improved, i.e., emissions in the eastern  
464 outskirts/suburbs are likely underestimated in the IER emissions model. The low modelled  
465  $\Delta XCO_2$  could also be due to overestimated horizontal dispersion in the model, which seems  
466 less likely. When comparing the mean modelled daily cycle of the days when observations  
467 exist with the mean diurnal cycle for all days within the field campaign period, we find that  
468 the days with observations do not significantly differ from those without observations (see  
469 Fig. 14). An investigation of typical diurnal variations of modelled  $\Delta XCO_2$  can only be  
470 performed to a limited degree with the observational data available. Within the large  
471 uncertainties, the modelled and observed  $\Delta XCO_2$  agree throughout the day. When analysing  
472 the modelled  $\Delta XCO_2$  components we also find that the observed daytime increases of  
473  $\Delta XCO_2$  are driven by  $CO_2$  added by urban FF  $CO_2$  burning and that the impact of FF is  
474 significantly higher at PIS (up to 1 ppm) than at MIT site (0.5 ppm) in the model., Our  
475 observations indicate that both sites have strong diurnal variations. As the biogenic



476 contribution is expected to be similar, this is another indication that the impact of FF  
477 emissions on the MIT site is larger than predicted by our modelling framework.

478 Different  $\Delta XCO_2$  diurnal variations can be found for other upwind-downwind site pairs, but  
479 they are all systematically driven by the locally-added  $CO_2$  from FFCO<sub>2</sub>.

480

## 481 **5 Conclusion and Outlook**

482 For the two-weeks field campaign we demonstrated the ability of a network of five  
483 EM27/SUN spectrometers, placed in the outskirts of Paris, to successfully track the  $XCO_2$   
484 changes due to the urban plume of the city. However, we also found that  $XCO_2$  cannot be  
485 easily linked to local emissions as, even in such a densely populated area,  $XCO_2$  is still  
486 significantly influenced by natural  $CO_2$  uptake during the growing season. Using a gradient  
487 approach, i.e., analysing the difference between  $XCO_2$  measured at upwind and downwind  
488 stations, greatly reduced the impact of remote  $CO_2$  sinks. Overall, the  $XCO_2$  variability  
489 modelled using our ECMWF-CHIMERE system with IER ( $1 \times 1 \text{ km}^2$ ) emissions data was  
490 found to be comparable with the observed variability and diurnal evolution of  $XCO_2$ , despite  
491 a significantly enhanced background for modelled  $XCO_2$ . Our modelling framework, run at a  
492  $2 \times 2 \text{ km}^2$  resolution over Paris also predicts that NEE and BC only significantly impacts  
493  $\Delta XCO_2$  during a few situations, specifically when meteorological conditions change making  
494 the concept of 'upwind' and 'downwind' not applicable. When comparing modelled and  
495 measured  $\Delta XCO_2$  we find strong correlations (Pearson's R) of 0.8 and 0.96 for PIS-RES and  
496 MIT-RES, respectively. This can be considered as an excellent degree of correlation as even  
497 a model simulation which used optimised fluxes, based on surface observation, showed  
498 correlations of 0.91 for its posterior results [Breon et al. 2015]. The offset between model  
499 and observations also diminished for  $\Delta XCO_2$  and the slope found between observed and  
500 modeled PIS-RES gradient is statistically in accordance with a 1:1 relationship ( $1.07 \pm 0.09$ ).

501 However, the slope of the MIT-RES  $XCO_2$  gradient of  $1.72 \pm 0.06$  suggests that the emission  
502 model could potentially be improved, unless this underestimation of  $\Delta XCO_2$  by the model is  
503 caused by overestimated dispersion in the model. It seems rather likely that the dispersion  
504 would cause a general spreading of emission plumes and not systematically underestimate  
505 emissions impacts from less densely populated, parts of Île-de-France. The data also  
506 confirm previous results by models that  $XCO_2$  gradients caused by a megacity do not  
507 exceed 2 ppm, which supports the previous requirement for satellite observations of less  
508 than 1 ppm precision on individual soundings, and biases lower than 0.5 ppm (Ciais et al.  
509 2015). The gradients are mainly caused by the transport of FFCO<sub>2</sub> emissions but,  
510 interestingly, during specific episodes, a significant contribution comes from biogenic fluxes,  
511 suggesting that these fluxes cannot be neglected even when using gradients.



512 Unfortunately, the duration of the campaign was relatively short, so that an in-depth analysis  
513 of mean daily cycles or the impact of ambient conditions (traffic conditions, temperature,  
514 solar insolation, etc.) on the observed gradient and underlying fluxes could be investigated  
515 here. Hence, future studies in Paris and elsewhere should aim to perform longer-term  
516 observations during different seasons, which will allow better understanding changes in  
517 biogenic and anthropogenic CO<sub>2</sub> fluxes. A remotely-controllable shelter for the EM27/SUN  
518 instrument is currently under development [Heinle and Chen, 2017]. This will considerably  
519 facilitate the establishment of permanent spectrometer arrays around cities and other  
520 sources of interest. Nevertheless, our study already indicates that such observations of  
521 urban XCO<sub>2</sub> and ΔXCO<sub>2</sub> contain original information to understand local sources and sinks  
522 and that the modelling framework used here is suitable to support their interpretation. An  
523 improved model will also be able to adjust or better model the background conditions and  
524 potentially use this type of observations to estimate local CO<sub>2</sub> fluxes using a Bayesian  
525 inversion scheme similar to the existing system based on in-situ observations for Paris  
526 [Staufner et al. 2016].

527 We expect that the previous successful collaboration in the framework of the Paris campaign  
528 will mark the permanent implementation of COCCON as a common framework for a French-  
529 Canadian-German collaboration on the EM27/SUN instrument. The acquisition of additional  
530 spectrometers is planned by several partners.

531

#### 532 **Acknowledgement:**

533 ECCO would like to thank Ray Nasser (CRD) and Yves Rochon (AQRD) for their internal  
534 review. The authors from LSCE acknowledge the support of the SATINV group of Frederic  
535 Chevallier. The authors from KIT acknowledge support from the Helmholtz Research  
536 Infrastructure ACROSS. The authors from LISA acknowledge support from the OSU-  
537 EFLUVE (Observatoire des Sciences de l'Univers-Enveloppes Fluides de la Ville à  
538 l'Exobiologie).

539

#### 540 **References**

541

- 542 Agustí-Panareda, A., Massart, S., Chevallier, F., Bousetta, S., Balsamo, G., Beljaars, A., Ciais, P.,  
543 Deutscher, N.M., Engelen, R., Jones, L. and Kivi, R., 2014. Forecasting global atmospheric CO<sub>2</sub>.  
544 Atmospheric Chemistry and Physics, 14(21), pp.11959-11983.  
545 AIRPARIF, 2016. Inventaire régional des émissions en Île-de-France Année de référence 2012 –  
546 éléments synthétiques, Edition Mai 2016, Paris, France. Last access Dec. 14th, 2017, available at:  
547 [https://www.airparif.asso.fr/\\_pdf/publications/inventaire-emissions-idf-2012-150121.pdf](https://www.airparif.asso.fr/_pdf/publications/inventaire-emissions-idf-2012-150121.pdf)



- 548 Ammoura, L., Xueref-Remy, I., Vogel, F., Gros, V., Baudic, A., Bonsang, B., Delmotte, M., Té, Y. and  
549 Chevallier, F., 2016. Exploiting stagnant conditions to derive robust emission ratio estimates for CO<sub>2</sub>,  
550 CO and volatile organic compounds in Paris. *Atmospheric Chemistry and Physics*, 16(24), pp.15653-  
551 15664.
- 552 Bréon, F.M., Broquet, G., Puygrenier, V., Chevallier, F., Xueref-Remy, I., Ramonet, M., Dieudonné,  
553 E., Lopez, M., Schmidt, M., Perrussel, O. and Ciais, P., 2015. An attempt at estimating Paris area CO  
554 2 emissions from atmospheric concentration measurements. *Atmospheric Chemistry and Physics*,  
555 15(4), pp.1707-1724. <https://doi.org/10.5194/acp-15-1707-2015>, 2015.
- 556 Broquet, G., Breon, F-M., Renault, E., Buchwitz, M., Reuter, M., Bovensmann, H., Chevallier, F., Wu  
557 L., and P. Ciais, 2017 in review.. The potential of satellite spectro-imagery for monitoring CO<sub>2</sub>  
558 emissions from large cities.
- 559 Boussetta, S., Balsamo, G., Beljaars, A., Panareda, A.A., Calvet, J.C., Jacobs, C., Hurk, B., Viterbo,  
560 P., Lafont, S., Dutra, E. and Jarlan, L., 2013. Natural land carbon dioxide exchanges in the ECMWF  
561 Integrated Forecasting System: Implementation and offline validation. *Journal of Geophysical*  
562 *Research: Atmospheres*, 118(12), pp.5923-5946.
- 563 Butz, A., Orphal, J., Checa-Garcia, R., Friedl-Vallon, F., von Clarmann, T., Bovensmann, H.,  
564 Hasekamp, O., Landgraf, H., Knigge, T., Weise, D., Sqalli-Houssini, O., and D. Kemper,  
565 Geostationary Emission Explorer for Europe (G3E): mission concept and initial performance  
566 assessment, *Atmos. Meas. Tech.*, 8, 4719-4734, 2015
- 567 Chen, J., Viatte, C., Hedelius, J. K., Jones, T., Franklin, J. E., Parker, H., Gottlieb, E. W., Wennberg,  
568 P. O., Dubey, M. K., and Wofsy, S. C., 2016. Differential column measurements using compact solar-  
569 tracking spectrometers, *Atmos. Chem. Phys.*, 16, 8479-8498, [https://doi.org/10.5194/acp-16-8479-](https://doi.org/10.5194/acp-16-8479-2016)  
570 2016, 2016.
- 571 Ciais, P., Crisp, D., Denier van der Gon, H., Engelen, R., Heimann, M., Janssens-Maenhout, G.,  
572 Rayner, P. and Scholze, M., 2015. Towards a European Operational Observing System to Monitor  
573 Fossil CO<sub>2</sub> Emissions. Final Report from the Expert Group, European Commission, October 2015.  
574 Available at [http://edgar.jrc.ec.europa.eu/news\\_docs/CO2\\_report\\_22-10-2015.pdf](http://edgar.jrc.ec.europa.eu/news_docs/CO2_report_22-10-2015.pdf) Accessed February  
575 6th, 2018
- 576 Dhakal, S., 2009. Urban energy use and carbon emissions from cities in China and policy  
577 implications, *Energy Policy* 37:4208-4219
- 578 Frey, M., F. Hase, T. Blumenstock, J. Groß, M. Kiel, G. Mengistu Tsidu, K. Schäfer, M. Kumar Sha,  
579 and J. Orphal, 2015. Calibration and instrumental line shape characterization of a set of portable FTIR  
580 spectrometers for detecting greenhouse gas emissions, *Atmos. Meas. Tech.*, 8, 3047-3057,  
581 doi:10.5194/amt-8-3047-2015
- 582 Frey, M., Sha, M.K., Hase, F., Kiel, M., Blumenstock, T., Harig, G., Surawicz, G., Deutscher,  
583 N.M., Shiomi, K., Franklin, J., Bösch, H., Chen, J., Grutter, M., Ohyama, H., Sun, Y., Butz,  
584 A., Mengistu Tsidu, G., Ene, D., Wunch, D., Song, C.Z., Garcia, O., Ramonet, M., Vogel, F.,  
585 and J. Orphal, Building the COllaborative Carbon Column Observing Network (COCCON):





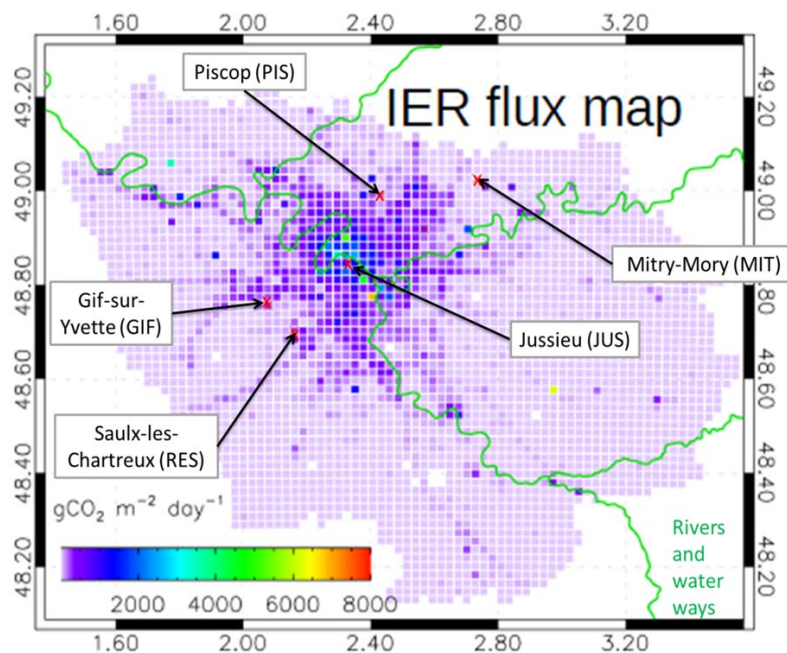
- 586 Long term stability and ensemble performance of the EM27/SUN Fourier transform  
587 spectrometer, Atmos. Meas. Tech. Diss, submitted, 2018
- 588 Gisi, M., F. Hase, S. Dohe, T. Blumenstock, A. Simon, and A. Keens, 2012. XCO<sub>2</sub>-measurements  
589 with a tabletop FTS using solar absorption spectroscopy, Atmos. Meas. Tech., 5, 2969-2980,  
590 doi:10.5194/amt-5-2969-2012
- 591 Hase, F., M. Frey, T. Blumenstock, J. Groß, M. Kiel, R. Kohlhepp, G. Mengistu Tsidu, K. Schäfer, M.  
592 K. Sha, and J. Orphal, 2015. Application of portable FTIR spectrometers for detecting greenhouse gas  
593 emissions of the major city Berlin, Atmos. Meas. Tech., 8, 3059-3068, doi:10.5194/amt-8-3059-2015
- 594 Hase, F., M. Frey, M. Kiel, T. Blumenstock, R. Harig, A. Keens, and J. Orphal, 2016. Addition of a  
595 channel for XCO observations to a portable FTIR spectrometer for greenhouse gas measurements,  
596 Atmos. Meas. Tech., 9, 2303-2313, doi:10.5194/amt-9-2303-2016
- 597 Hedelius, J. K., Viatte, C., Wunch, D., Roehl, C. M., Toon, G. C., Chen, J., Jones, T., Wofsy, S. C.,  
598 Franklin, J. E., Parker, H., Dubey, M. K., and Wennberg, P. O., 2016. Assessment of errors and  
599 biases in retrievals of X<sub>CO<sub>2</sub></sub>, X<sub>CH<sub>4</sub></sub>, X<sub>CO</sub>, and X<sub>N<sub>2</sub>O</sub> from a 0.5 cm<sup>-1</sup> resolution solar-viewing spectrometer,  
600 Atmos. Meas. Tech., 9, 3527-3546, <https://doi.org/10.5194/amt-9-3527-2016>
- 601 Heinle, L. and Chen, J., 2017 in review. Automated Enclosure and Protection System for Compact  
602 Solar-Tracking Spectrometers, Atmos. Meas. Tech. Discuss., <https://doi.org/10.5194/amt-2017-292>
- 603 IEA, International Energy Agency, 2008, World Energy Outlook, IEA Publications, Paris, France ISBN:  
604 978926404560-6
- 605 IPCC-WG1, Climate Change 2013: The Physical Science Basis. Contribution of Working Group I to  
606 the Fifth Assessment Report of the Intergovernmental Panel on Climate Change [Stocker, T.F., D.  
607 Qin, G.-K. Plattner, M. Tignor, S.K. Allen, J. Boschung, A. Nauels, Y. Xia, V. Bex and P.M. Midgley  
608 (eds.)]. Cambridge University Press, Cambridge, United Kingdom and New York, NY, USA, 1535 pp
- 609 IPCC-WG3, Climate Change 2014: Mitigation of Climate Change. Contribution of Working Group III to  
610 the Fifth Assessment Report of the Intergovernmental Panel on Climate Change [Edenhofer, O., R.  
611 Pichs-Madruga, Y. Sokona, E. Farahani, S. Kadner, K. Seyboth, A. Adler, I. Baum, S. Brunner, P.  
612 Eickemeier, B. Kriemann, J. Savolainen, S. Schlömer, C. von Stechow, T. Zwickel and J.C. Minx  
613 (eds.)]. Cambridge University Press, Cambridge, United Kingdom and New York, NY, USA
- 614 Janardanan, R., S. Maksyutov, T. Oda, M. Saito, J. W. Kaiser, A. Ganshin, A. Stohl, T. Matsunaga, Y.  
615 Yoshida, and T. Yokota (2016), Comparing GOSAT observations of localized CO<sub>2</sub> enhancements by  
616 large emitters with inventory-based estimates, Geophys. Res. Lett., 43, 3486–3493,  
617 doi:10.1002/2016GL067843.
- 618 Jones, N., 2013, Troubling milestone for CO<sub>2</sub>. Nature Geoscience 6, no. 8, 589-589.
- 619 Keppel-Aleks, G., Toon, G.C., Wennberg, P.O. and Deutscher, N.M., 2007. Reducing the impact of  
620 source brightness fluctuations on spectra obtained by Fourier-transform spectrometry. Applied optics,  
621 46(21), pp.4774-4779.
- 622 Keppel-Aleks, G., P. O. Wennberg, and T. Schneider (2011), Sources of variations in total column  
623 carbon dioxide, Atmospheric Chemistry and Physics, 11(8), 3581-3593, doi:10.5194/acp-11-3581-  
624 2011



- 625 Klappenbach, F., Bertleff, M., Kostinek, J., Hase, F., Blumenstock, T., Agusti-Panareda, A., Razinger,  
626 M., and Butz, A., 2015. Accurate mobile remote sensing of XCO<sub>2</sub> and XCH<sub>4</sub> latitudinal transects from  
627 aboard a research vessel, *Atmos. Meas. Tech.*, 8, 5023-5038, [https://doi.org/10.5194/amt-8-5023-](https://doi.org/10.5194/amt-8-5023-2015)  
628 2015
- 629 Kort, E. A., C. Frankenberg, C. E. Miller, and T. Oda (2012), Space-based observations of megacity  
630 carbon dioxide, *Geophys. Res. Lett.*, 39, L17806, doi:10.1029/2012GL052738.
- 631 Latoska, A., 2009. Erstellung eines räumlich hoch aufgelösten Emissionsinventar von  
632 Luftschadstoffen am Beispiel von Frankreich im Jahr 2005, Master's thesis, Institut für  
633 Energiewirtschaft und Rationelle Energieanwendung, Universität Stuttgart, Stuttgart, Germany
- 634 Messerschmidt, J., Geibel, M. C., Blumenstock, T., Chen, H., Deutscher, N. M., Engel, A., Feist, D.  
635 G., Gerbig, C., Gisi, M., Hase, F., Katrynski, K., Kolle, O., Lavrič, J. V., Notholt, J., Palm, M.,  
636 Ramonet, M., Rettinger, M., Schmidt, M., Sussmann, R., Toon, G. C., Truong, F., Warneke, T.,  
637 Wennberg, P. O., Wunch, D., and Xueref-Remy, I., 2011. Calibration of TCCON column-averaged  
638 CO<sub>2</sub>: the first aircraft campaign over European TCCON sites, *Atmos. Chem. Phys.*, 11, 10765-10777,  
639 <https://doi.org/10.5194/acp-11-10765-2011>
- 640 Nassar, R., Hill, T.G., McLinden, C.A., Wunch, D., Jones, D.B.A. and D. Crisp, 2017. Quantifying CO<sub>2</sub>  
641 emissions from individual power plants from space, *JGR*, 44, 19, 10045-1053.
- 642 Nassar, R., Napier-Linton, L., Gurney, K.R., Andres, R.J., Oda, T., Vogel, F.R. and Deng, F., 2013.  
643 Improving the temporal and spatial distribution of CO<sub>2</sub> emissions from global fossil fuel emission data  
644 sets. *Journal of Geophysical Research: Atmospheres*, 118(2), pp.917-933.
- 645 O'Brien, D.M., Polonsky, I.N., Utembe, S.R. and Rayner, P.J., 2016. Potential of a geostationary  
646 geoCARB mission to estimate surface emissions of CO<sub>2</sub>, CH<sub>4</sub> and CO in a polluted urban  
647 environment: case study Shanghai. *Atmospheric Measurement Techniques*, 9(9), p.4633.
- 648 Olivier, J. and G. Janssens-Maenhout, CO<sub>2</sub> Emissions from Fuel Combustion – 2012 Edition, IEA  
649 CO<sub>2</sub> report 2012, Part III, Greenhouse-Gas Emissions, ISBN 978-92-64-17475-7
- 650 Rötzer, T, and F-M. Chmielewski. 2001. Phenological maps of Europe., *Climate research* 18.3, 249-  
651 257.
- 652 Schwandner, F.M., Gunson, M.R., Miller, C.E., Carn, S.A., Eldering, A., Krings, T., Verhulst, K.R.,  
653 Schimel, D.S., Nguyen, H.M., Crisp, D. and O'dell, C.W., 2017. Spaceborne detection of localized  
654 carbon dioxide sources. *Science*, 358(6360), p.eaam5782.
- 655 Schneider, M. and Hase, F.: Ground-based FTIR water vapour profile analyses, *Atmos. Meas. Tech.*,  
656 2, 609–619, doi:10.5194/amt-2-609-2009, 2009.
- 657 Staufer, J., Broquet, G., Bréon, F.M., Puygrenier, V., Chevallier, F., Xueref-Rémy, I., Dieudonné, E.,  
658 Lopez, M., Schmidt, M., Ramonet, M. and Perrussel, O., 2016. The first 1-year-long estimate of the  
659 Paris region fossil fuel CO<sub>2</sub> emissions based on atmospheric inversion. *Atmospheric Chemistry and*  
660 *Physics*, 16(22), pp.14703-14726.
- 661 Turnbull, J.C., Sweeney, C., Karion, A., Newberger, T., Lehman, S.J., Tans, P.P., Davis, K.J.,  
662 Lauvaux, T., Miles, N.L., Richardson, S.J. and Cambaliza, M.O., 2015. Toward quantification and  
663 source sector identification of fossil fuel CO<sub>2</sub> emissions from an urban area: Results from the INFLUX  
664 experiment. *Journal of Geophysical Research: Atmospheres*, 120(1), pp.292-312.



- 665 Vogel, F.R., Thiruchittampalam, B., Theloke, J., Kretschmer, R., Gerbig, C., Hammer, S. and Levin, I.,  
666 2013. Can we evaluate a fine-grained emission model using high-resolution atmospheric transport  
667 modelling and regional fossil fuel CO<sub>2</sub> observations?. *Tellus B: Chemical and Physical Meteorology*,  
668 65(1), p.18681.
- 669 Wunch, D., Toon, G.C., Blavier, J.F.L., Washenfelder, R.A., Notholt, J., Connor, B.J., Griffith, D.W.T.,  
670 Sherlock, V. and Wennberg, P.O., 2011. The total carbon column observing network, *Philos. T. Roy.*  
671 *Soc. A*, 369, 2087–2112.
- 672 Wunch, D., Toon, C., Wennberg, O., Wofsy, C., Stephens, B., Fischer, L., Uchino, O., Abshire, B.,  
673 Bernath, P., Biraud, C. and Blavier, F., 2010. Calibration of the total carbon column observing network  
674 using aircraft profile data. *Atmospheric Measurement Techniques*, 3(5), pp.1351-1362.
- 675 Xueref-Remy, I., Dieudonné, E., Vuillemin, C., Lopez, M., Lac, C., Schmidt, M., Delmotte, M.,  
676 Chevallier, F., Ravetta, F., Perrussel, O., Ciais, P., Bréon, F.-M., Broquet, G., Ramonet, M., Spain, T.  
677 G., and Ampe, C.: Diurnal, synoptic and seasonal variability of atmospheric CO<sub>2</sub> in the Paris megacity  
678 area, *Atmos. Chem. Phys. Discuss.*, <https://doi.org/10.5194/acp-2016-218>, accepted in ACP.

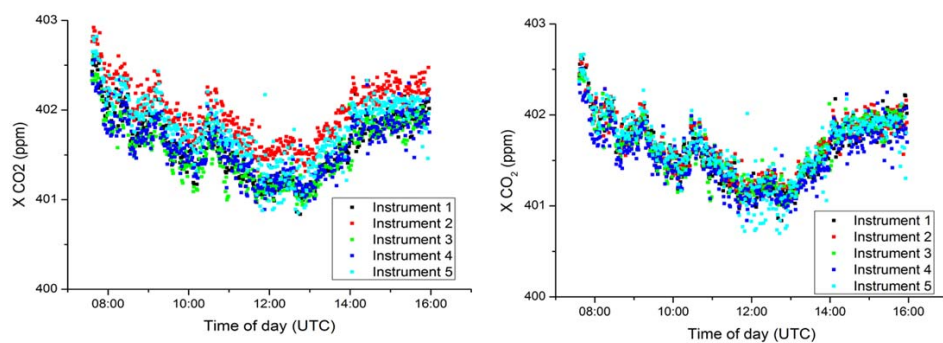


679

680

681

**Figure 1. CO<sub>2</sub> emissions in the Île-de-France region according to the IER emission inventory. Measurement sites are indicated by red crosses**

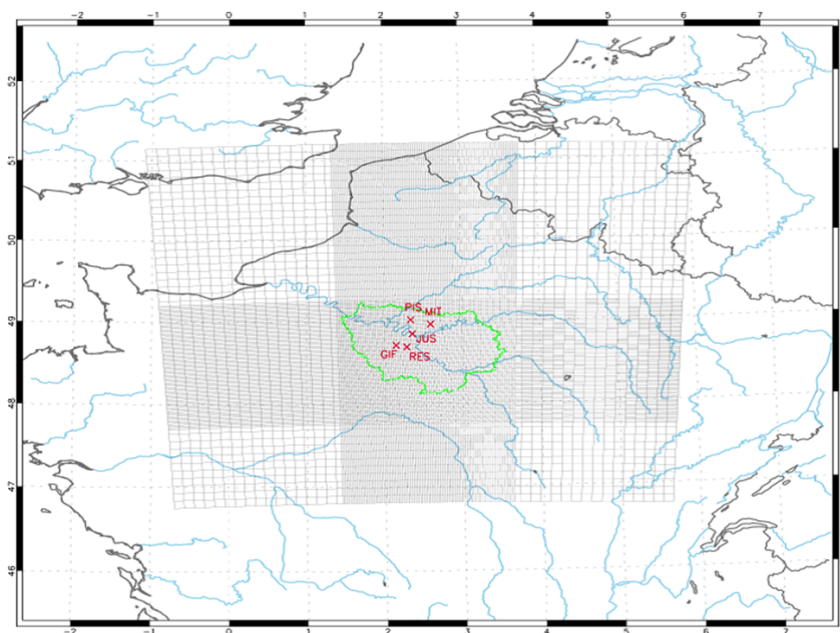


682

683 **Figure 2. Sample parallel measurements of the five EM27/SUN instruments in**

684 **Karlsruhe for raw data (left panel) and the data with the applied correction (right**

685 **panel) taken on April 15<sup>th</sup>, 2015.**

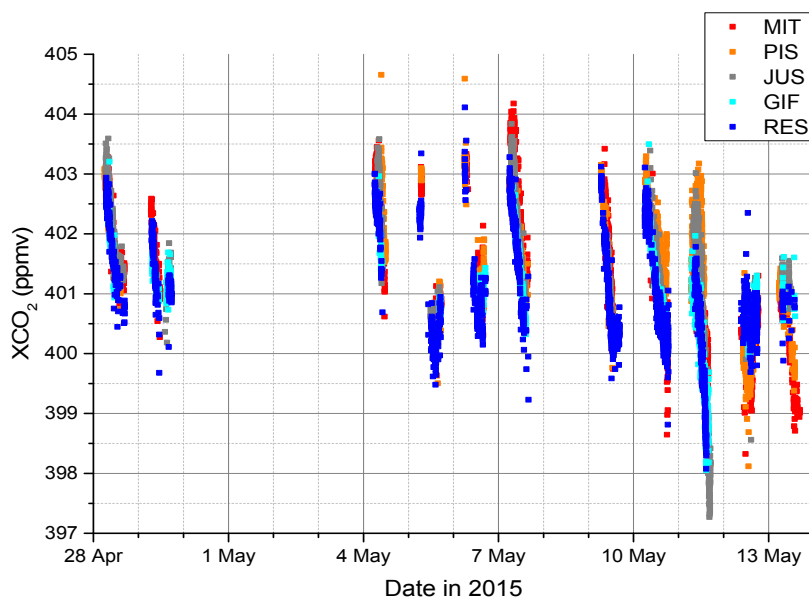


686

687

688

**Figure 3. Modelling domain and numerical grid configuration of CHIMERE with a zoom on the Île-de-France region at 2 x 2 km<sup>2</sup>.**

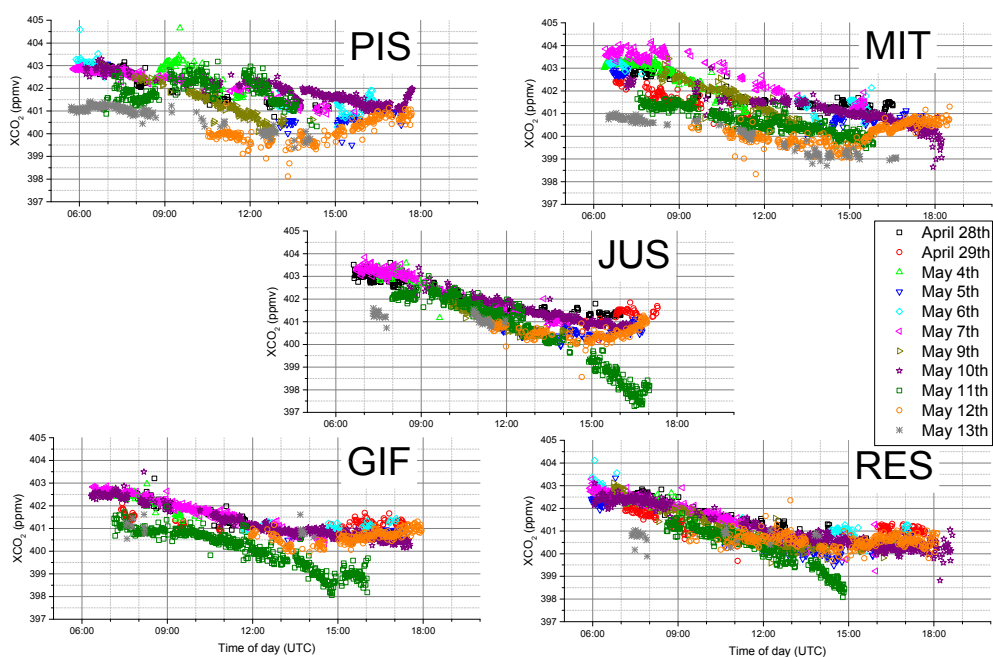


689

690

691

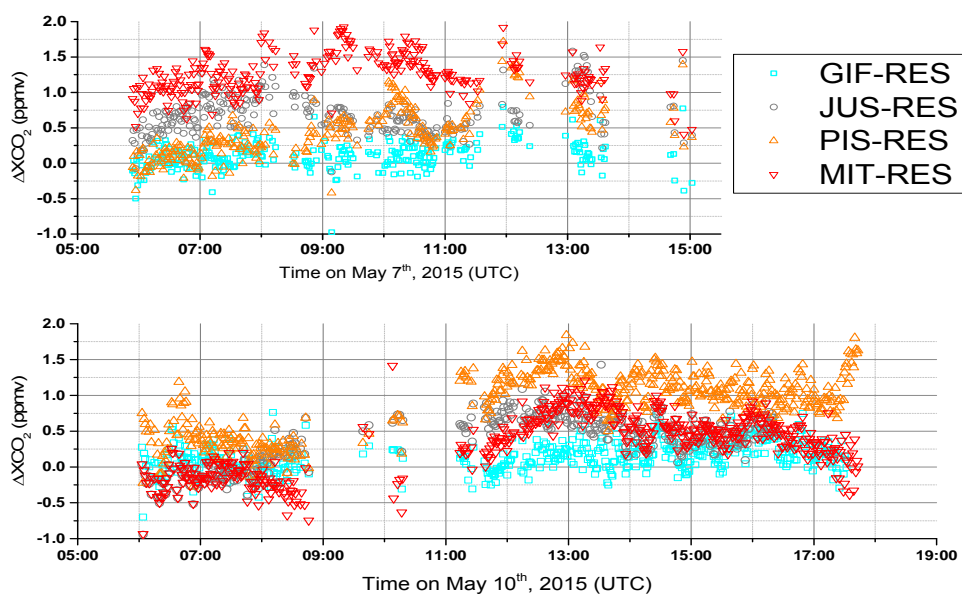
**Figure 4. Time series of observed XCO<sub>2</sub> in the Parisian region for all five sites (all valid data of ~1 minute averages).**



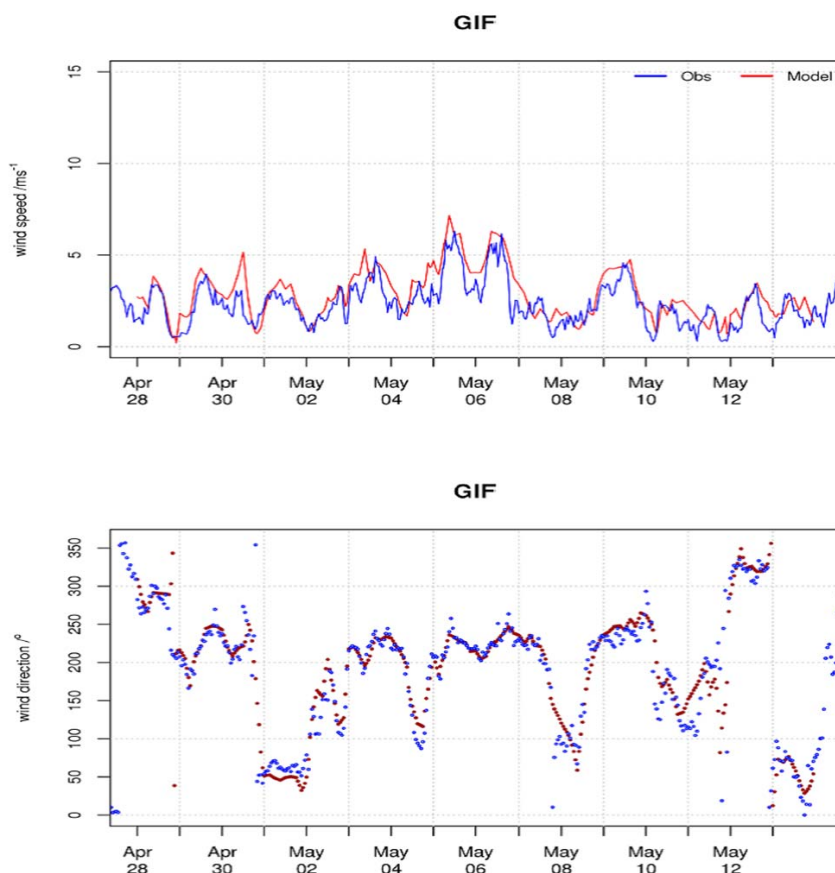
692  
693

Figure 5. Time series of observed XCO<sub>2</sub> in the Parisian region sorted by station





**Figure 6. Observed spatial gradients of XCO<sub>2</sub> for May 7<sup>th</sup> (southwesterly winds) and May 10<sup>th</sup> (southerly winds)**

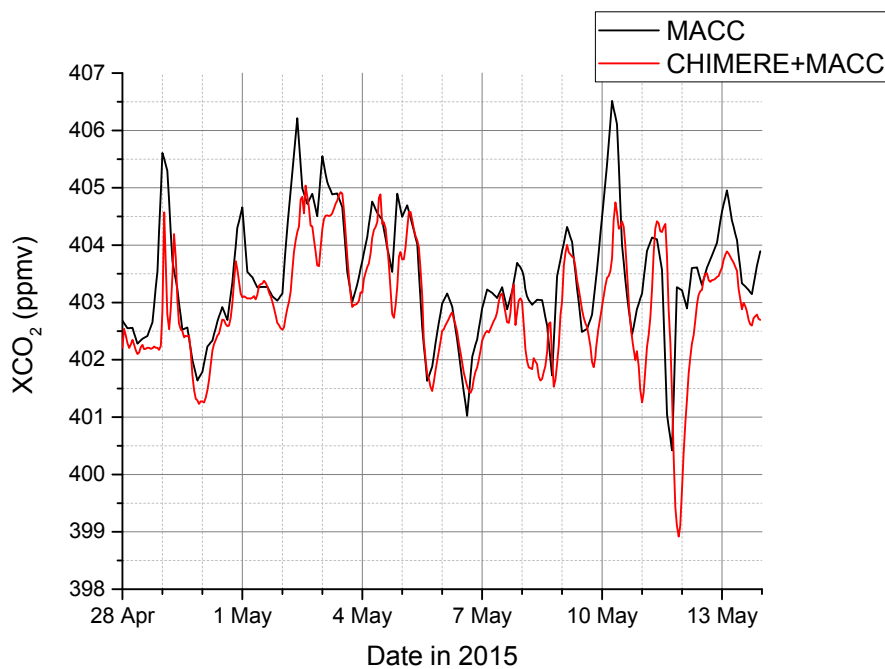


697

698

699

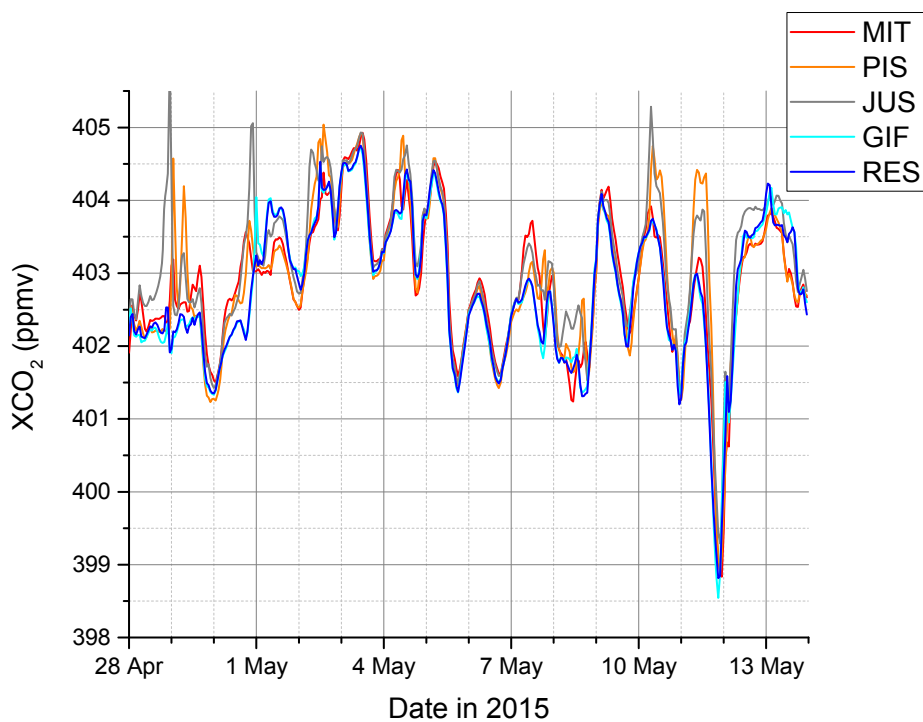
**Figure 7. Comparison of modelled and observed wind speeds and directions at the Gif-Sur-Yvette measurement site**



700

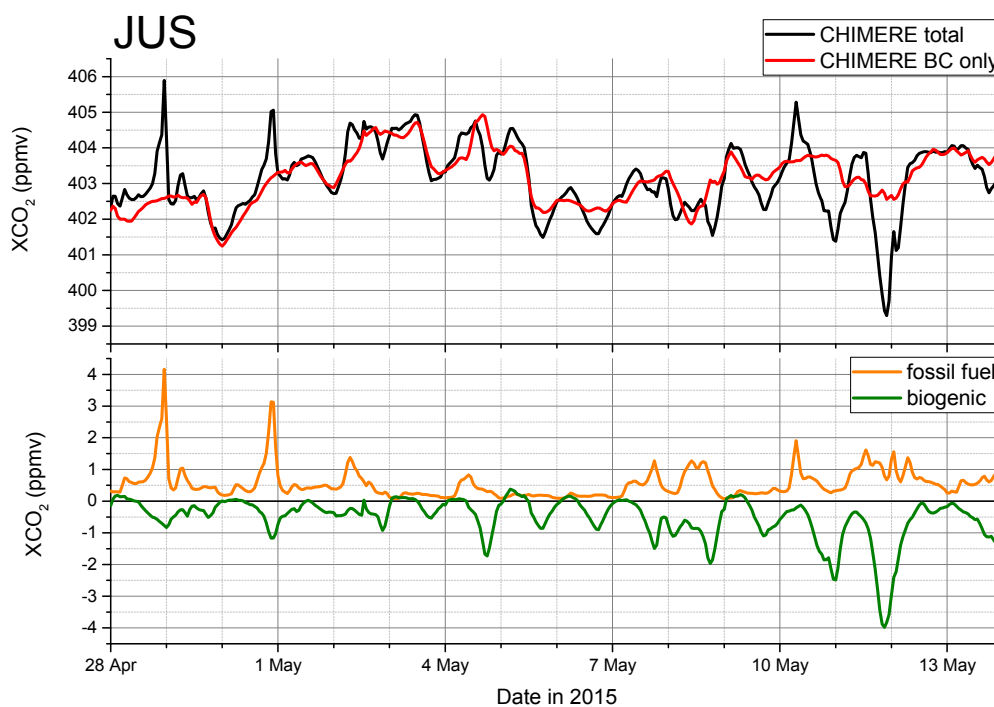
701 **Figure 8. Comparison of modelled XCO<sub>2</sub> from ECWMF-CAMS (15 x 15 km<sup>2</sup>) with**

702 **CHIMERE simulation (inner domain, 2 x 2 km<sup>2</sup>) for JUS.**



703

704 **Figure 9. Modelled XCO<sub>2</sub> for all stations**



705

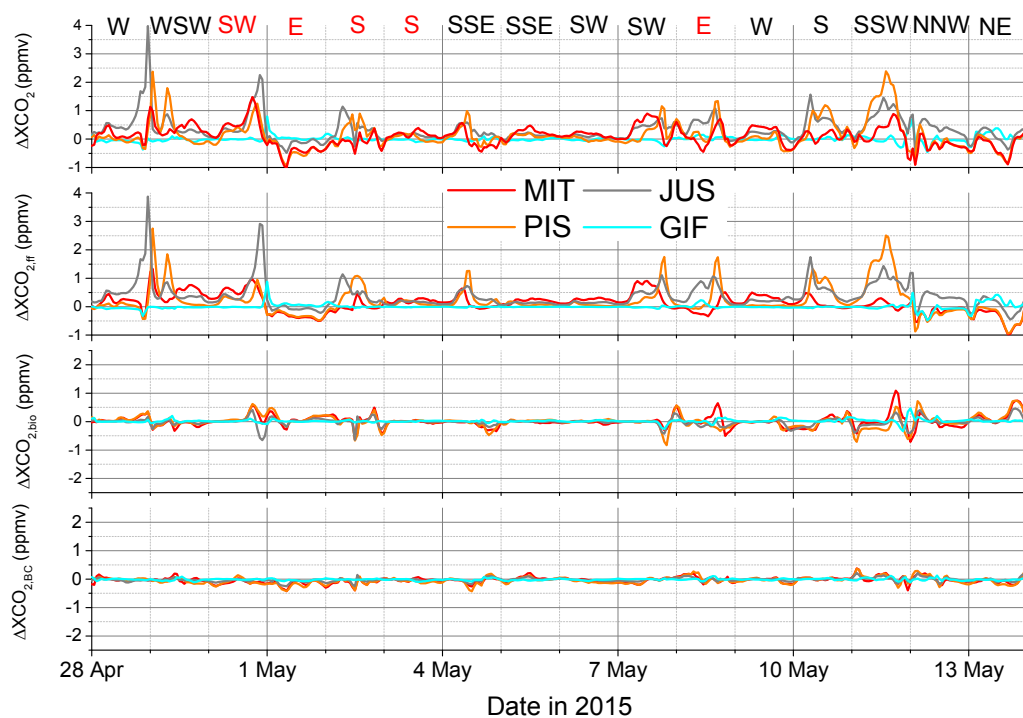
706

707

708

709

**Figure 10: Time series of  $XCO_2$  and related fluxes for JUS. The top panel provides a comparison of modelled total  $XCO_2$  and  $XCO_2$  variations due to changes in boundary conditions. The lower panel shows the contribution of the different flux components, namely fossil fuel  $CO_2$  emissions and biogenic fluxes.**

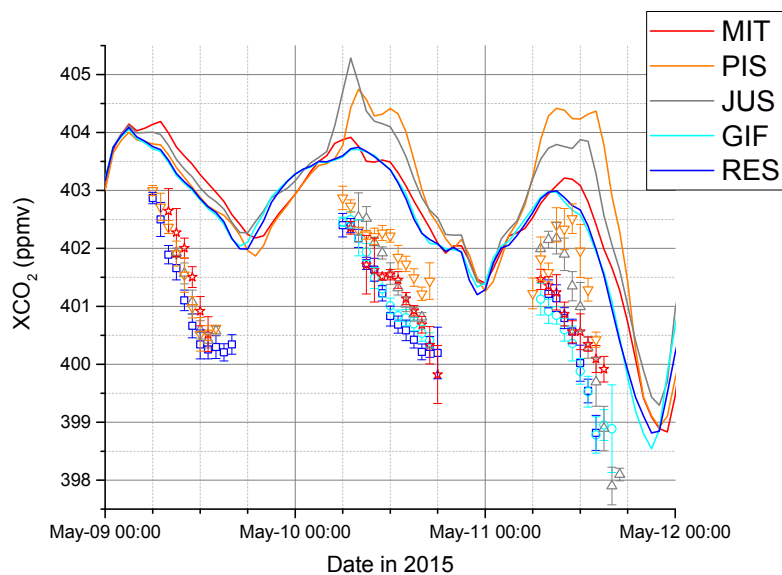


710

711 **Figure 11. Modelled XCO<sub>2</sub> gradients for each station relative to RES. The dominant**

712 **wind conditions for each day given at the top of the figure and days without**

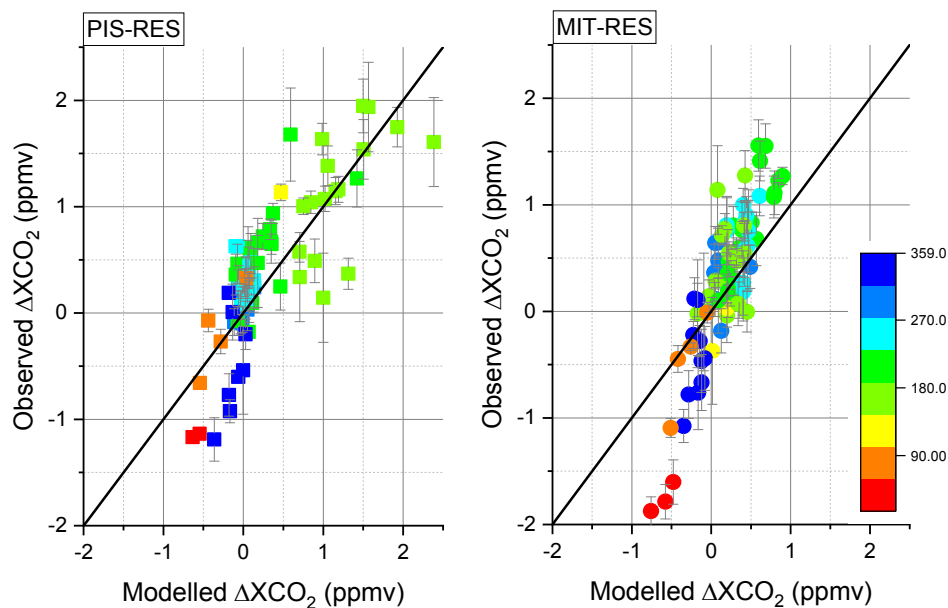
713 **observations due to precipitation are in red.**



714

715 **Figure 12. Comparison of modelled (solid lines) and observed hourly averaged XCO<sub>2</sub>**

716 **(symbols) with standard deviations as error bars.**



717

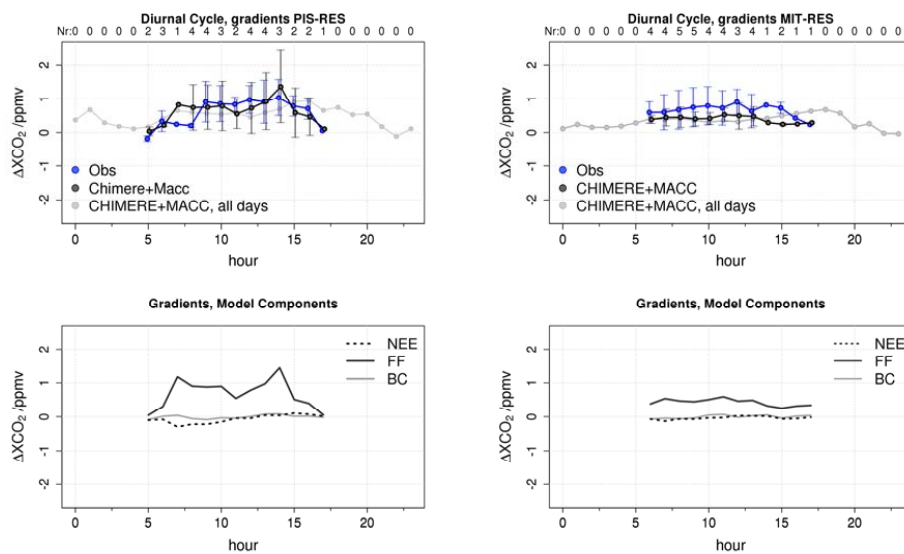
718 **Figure 13. Comparison of modelled and observed hourly averaged  $\Delta XCO_2$  for**

719 **gradients between PIS and RES (left) and MIT and RES (right), with standard**

720 **deviations as vertical bars and the points color coded by wind direction from 0 to 359**

721 **degrees.**





722

723

724 **Figure 14. Comparison of modelled and observed mean daily cycle of hourly averaged**  
 725  **$\Delta XCO_2$  of PIS with RES (top left) and of MIT with RES (top right) during the campaign**  
**and the modelled contribution of different  $CO_2$  sources/sinks (bottom panels).**



Location	ID	Lat (deg)	Lon (deg)	Position
Piscop	PIS	49.019	2.347	20 km NNW of JUS
Mitry-Mory	MIT	48.984	2.626	25 km NW of JUS
Jussieu	JUS	48.846	2.356	Paris city centre
Saulx-les-Chartreux	RES	48.688	2.284	20 km SSW of JUS
Gif-Sur-Yvette	GIF	48.708	2.148	20 km SW of JUS

726 Table 1. Location of FTIR measurement instruments during the field campaign



Instrument	XCO <sub>2</sub> factor Berlin	XCO <sub>2</sub> factor before Paris	XCO <sub>2</sub> factor after Paris
1	1.0000 (0.0003)	1.0000 (0.0003)	1.0000 (0.0003)
2	0.9992 (0.0003)	0.9991 (0.0003)	0.9992 (0.0003)
3	1.0002 (0.0003)	1.0001 (0.0004)	1.0000 (0.0005)
4	0.9999 (0.0003)	1.0000 (0.0004)	1.0000 (0.0004)
5	0.9996 (0.0003)	0.9995 (0.0003)	0.9995 (0.0003)

727 Table 2. Normalisation factors for the five EM27/SUN instruments derived during  
728 measurements before and after the Paris field campaign. Values in parentheses are  
729 standard deviations. Measurements of instrument 1 were arbitrarily chosen as  
730 reference from which the others were scaled. . The calibration factors from a previous  
731 field campaign in Berlin [Hase et al. 2015] are also shown. Calibration factors between  
732 the two field campaigns agree well within 0.02 % (~0.08 ppm) for all instruments.



Date	No. of observations					Quality	Wind speed (m s <sup>-1</sup> )	Wind direction
	MIT	GIF	PIS	RES	JUS			
28 Apr 2015 (Tu)	179	102	178	199	234	++	4	W
29 Apr 2015 (We)	110	124	0	161	53	+	5	SW-W
04 Mai 2015 (Mo)	194	85	96	163	83	+	6	S-SE
05 Mai 2015 (Tu)	77	27	85	185	92	+	8	S-SW
06 Mai 2015 (We)	81	88	87	139	0	+	8	SW
07 Mai 2015 (Th)	169	313	252	286	238	+++	3	SW
09 Mai 2015 (Sa)	179	0	181	289	149	++	6	W
10 Mai 2015 (Su)	325	478	362	542	282	++++	3	S
11 Mai 2015 (Mo)	410	431	251	298	413	++++	3	SSW
12 Mai 2015 (Tu)	324	222	230	326	203	+++	4	NNW
13 Mai 2015 (We)	159	18	182	28	56	+	4	NE

733 **Table 3.** Summary of all measurement days with the number of observations at each  
734 of the sites, Mitry Mory (MIT) , Gif Sur Yvette (GIF), Piscop (PIS), Saulx-les-Chartreux  
735 (RES), Jussieu (JUS), the overall quality ranking of each day according to the number  
736 of available observations and temporal coverage (with classification from poor to  
737 great: +, ++, +++, ++++), and the ground-level wind speed and direction.



	Total obs	Mean (ppm)	STD (ppm)	Quartile1 (ppm)	Median (ppm)	Quartile3 (ppm)
RES	2616	401.11	0.93	400.44	400.88	401.96
GIF	1888	401.05	0.92	400.94	400.94	401.58
JUS	1803	401.33	1.17	401.31	401.31	402.04
PIS	1904	401.62	0.95	401.03	401.59	402.44
MIT	2207	401.26	1.15	401.11	401.11	401.95

738 **Table 4.** Statistics of observed XCO<sub>2</sub> 1-minute averages for all sites